Numerical Investigation of an Electrochemically Induced Tagging in a Nanospray for Protein Analysis

4 AUTHORS, INCLUDING:

Henrik Jensen
University of Copenhagen
88 PUBLICATIONS **1,858** CITATIONS

SEE PROFILE

Hubert H Girault
École Polytechnique Fédérale de Lausanne
559 PUBLICATIONS **14,028** CITATIONS

SEE PROFILE

Numerical Investigation of an Electrochemically Induced Tagging in a Nanospray for Protein Analysis

Tatiana C. Rohner, Jacques Josserand, Henrik Jensen, and Hubert H. Girault*

Laboratoire d'Electrochimie Physique et Analytique, Institut de Chimie Moleculaire et Biologique, Ecole Polytechnique Fédérale de Lausanne, CH-1015 Lausanne, Switzerland

An on-line tagging of target species is simulated using the finite element method. A numerical model of an electrochemical EC$_{2X}$E mechanism in a flow channel cell has been developed, corresponding to the electrochemical generation of a probe and the subsequent homogeneous reaction with the target. The kinetic and convective aspects are validated on short electrode geometries before taking into account the depletion of the target species. The model is then assessed according to previous experimental results on the on-line tagging of proteins. The occurrence and the efficiency of the on-line tagging are studied for both pressure-driven and electroosmotic flows. The involved phenomena including kinetic aspects are described in detail. Finally, optimal conditions for an effective quantitative tagging are discussed.

Since the 1980s, a lot of effort has been made in the numerical characterization of microband electrodes for voltammetric studies under diffusion-limited[1−7] as well as diffusion convection-limited mass transport.[8−19] This type of electrode offers many advantages in terms of electrochemical behavior, and their ease of fabrication (by photolithography or even simply by sealing metal films between two insulating layers) has led to applications in many analytical methods.[20] Recently, a method based on photoablation of polymers for the production of microband electrodes has been developped.[21] These channel electrodes have been introduced in many analytical apparatus, such as capillary electrophoresis using electrochemical detection[22] or a nanospray interface.[23] In the latter, a thick-film microelectrode is embedded at the bottom of a microchannel, in which an analyte solution flows toward the open end. A high voltage is applied between the electrode and a mass spectrometer (MS) resulting in electrospray (ESI) generation. If a positive potential is applied to the microelectrode, it can be considered as an anode and the mass spectrometer is then the cathode. The whole system can be regarded as a special kind of electrolytic cell.[24] The convective transport of the ions occurs first in the solution (i.e., in the microchannel), then as a result of the electrospray process, charged droplets are ejected from the channel outlet. The ions are subsequently transferred to the gas phase (evaporation and fission of the droplets) and guided to the MS thanks to the applied electric field. The conduction in the gap is thus controlled by the flow of gas-phase ions generated from the nanospray outlet to the MS. When a positive potential is applied, electroactive species (i.e., the analytes[25−27] or the solvents[28]) may undergo oxidation at the electrode in the channel,[29] or the ESI electrode itself may be electrolyzed.[24] Taking advantage

* Corresponding author: (e-mail) hubert.girault@epfl.ch; (phone) + 41 21 693 31 51; (fax) + 41 21 693 36 67.

(1) Alden, J. A.; Booth, J.; Compton, R. G.; Dryfe, R. A. W.; Sanders, G. H. W. *J. Electroanal. Chem.* **1995**, *389*, 45−54.

(2) Coen, S.; Cope, D. K.; Tallman, D. E. *J. Electroanal. Chem.* **1986**, *215*, 29−48.

(3) Aixill, W. J.; Alden, J. A.; Prieto, F.; Waller, G. A.; Compton, R. G.; Rueda, M. *J. Phys. Chem. B* **1998**, *102*, 1515−1521.

(4) Alden, J. A.; Compton, R. G. *Electroanalysis* **1996**, *8*, 30−33.

(5) Amatore, C. A.; Fosset, B.; Deakin, M. R.; Wightman, R. M. *J. Electroanal. Chem.* **1987**, *225*, 33−48.

(6) Deakin, M. R.; Wightman, R. M.; Amatore, C. A. *J. Electroanal. Chem.* **1986**, *215*, 49−61.

(7) Seddon, B. J.; Girault, H. H.; Eddowes, M. J. *J. Electroanal. Chem.* **1989**, *266*, 227−238.

(8) Unwin, P. R.; Compton, R. G. *J. Electroanal. Chem.* **1988**, *245*, 287−298.

(9) Alden, J. A.; Compton, R. G. *J. Electroanal. Chem.* **1996**, *402*, 1−10.

(10) Alden, J. A.; Compton, R. G. *J. Electroanal. Chem.* **1996**, *404*, 27−35.

(11) Bidwell, M. J.; Alden, J. A.; Compton, R. G. *J. Electroanal. Chem.* **1996**, *417*, 119−128.

(12) Ball, J. C.; Compton, R. G. *Electroanalysis* **1997**, *9*, 1305−1310.

(13) Ferrigno, R.; Brevet, P. F.; Girault, H. H. *J. Electroanal. Chem.* **1997**, *430*, 235−242.

(14) Ferrigno, R.; Josserand, J.; Brevet, P. F.; Girault, H. H. *Electrochim. Acta* **1998**, *44*, 587−595.

(15) Bidwell, M. J.; Alden, J. A.; Compton, R. G. *J. Electroanal. Chem.* **1996**, *414*, 247−251.

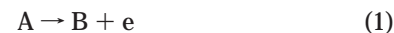(16) Bidwell, M. J.; Alden, J. A.; Compton, R. G. *Electroanalysis* **1997**, *9*, 383−389.

(17) Compton, R. G.; Dryfe, R. A. W.; Alden, J. A.; Rees, N. V.; Dobson, P. J.; Leigh, P. A. *J. Phys. Chem.* **1994**, *98*, 1270−1275.

(18) Rees, N. V.; Alden, J. A.; Dryfe, R. A. W.; Coles, B. A.; Compton, R. G. *J. Phys. Chem.* **1995**, *99*, 14813−14818.

(19) Stevens, N. P. C.; Fisher, A. C. *J. Phys. Chem. B* **1997**, *101*, 8259−8263.

(20) Cooper, J. A.; Compton, R. G. *Electroanalysis* **1998**, *10*, 141−155.

(21) Rossier, J. S.; Roberts, M. A.; Ferrigno, R.; Girault, H. H. *Anal. Chem.* **1999**, *71*, 4294−4299.

(22) Rossier, J. S.; Ferrigno, R.; Girault, H. H. *J. Electroanal. Chem.* **2000**, *492*, 15−22.

(23) Rohner, T. C.; Rossier, J. S.; Girault, H. H. *Anal. Chem.* **2001**, *73*, 5353−5357.

(24) Blades, A. T.; Ikonomou, M. G.; Kebarle, P. *Anal. Chem.* **1991**, *63*, 2109−2114.

(25) Morand, K.; Talbo, G.; Mann, M. *Rapid Commun. Mass Spectrom.* **1993**, *7*, 738−743.

(26) Van Berkel, G. J. *J. Am. Soc. Mass Spectrom.* **2000**, *11*, 951−960.

(27) Smith, A. D.; Moini, M. *Anal. Chem.* **2001**, *73*, 240−246.

(28) Van Berkel, G. J.; Zhou, F. M.; Aronson, J. T. *Int. J. Mass Spectrom. Ion Processes* **1997**, *162*, 55−67.

(29) de la Mora, J. F.; Van Berkel, G. J.; Enke, C. G.; Cole, R. B.; Martinez-Sanchez, M.; Fenn, J. B. *J. Mass Spectrom.* **2000**, *35*, 939−952.

of this electrolytic behavior, a method based on the oxidation of hydroquinone has been developed to tag free cysteine residues in proteins immediately prior to mass spectrometry analyses.[30] This on-line modification allows a direct identification of the number of free cysteine units in proteins thanks to the MS analyses performed right after the tagging process. The cysteine residue is quite common (only 10% of the human proteome is cysteine-free), and it is, however, of utmost importance because it is involved in many essential biological events. From an analytical point of view, exact knowledge of the cysteine content greatly increases the confidence in the overall protein identification procedure.[31]

For the electrochemically induced cysteine tagging, a solution containing proteins and hydroquinone is infused in the microchannel. Hydroquinone undergoes an oxidation at the channel electrode (A → B), and the product, benzoquinone, reacts with the free cysteines of the protein (B + X → C). The adduct is formed in a reduced state and, hence, can be reoxidized at the same microelectrode (C → E). This on-line electrochemical tagging corresponds therefore to an $EC_{2X}E$ mechanism. This mechanism has been investigated for other hydrodynamic steady-state techniques using finite difference modelization.[32] Particularly, the electrochemically induced reaction of L-cysteine with acetamidophenol (paracetamol) has already been investigated and shown to follow an $EC_{2X}E$ pathway.[33] A good agreement between experimental and numerical results for the voltammetric sensing of thiols was observed. To study the quantitative yield of the whole reaction, a finite element model of the electrochemically induced tagging in a 2D microchannel has been developed using the equation generator of the Flux-Expert software. After initial validations, ECE and $EC_{2X}E$ mechanisms are described and the effect of the target concentration is evaluated. The present model is then checked against previous experimental results. Finally, convection and kinetic effects are investigated, unraveling all the phenomena involved in the electrochemically induced tagging.

THEORY

The phenomena described above are set out as a simplified model, where two species A and X are continuously introduced in a channel containing a microelectrode at the bottom. A is the first species to be oxidized at the electrode, producing B (1), which will further react homogeneously with X (2). The produced species C can then be oxidized at the same electrode (4). As said above, the (1) to (2) to (4) sequence results in an $EC_{2X}E$ mechanism, where the homogeneous reaction is characterized by a kinetic rate constant K'. Moreover, side reactions, which have been pointed out in the case of the cysteine with quinones tagging,[30,34] are not taken into account in the present model.

(30) Rohner, T. C.; Rossier, J. S.; Girault, H. H. *Electrochem. Commun.* **2002**, *4*, 695−700.
(31) Sechi, S.; Chait, B. T. *Anal. Chem.* **1998**, *70*, 5150−5158.
(32) Brookes, B. A.; Lawrence, N. S.; Compton, R. G. *J. Phys. Chem. B* **2000**, *104*, 11258−11267.
(33) Brookes, B. A.; White, P. C.; Lawrence, N. S.; Compton, R. G. *J. Phys. Chem. B* **2001**, *105*, 6361−6366.
(34) Roussel, C.; Rohner, T. C.; Jensen, H.; Girault, H. H. *ChemPhysChem* **2003**, *4*, 200−206.
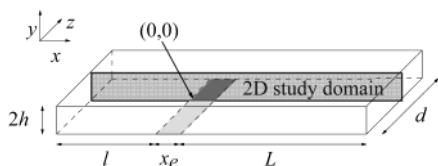
$$A \rightarrow B + e \tag{1}$$

$$B + X \xrightarrow{K'} C \tag{2}$$

or

$$B \xrightarrow{k} C \tag{3}$$

$$C \rightarrow E + e \tag{4}$$

$$K' c_x^0 = k \tag{5}$$

To validate and compare the model with the literature, an ECE mechanism (1) to (3) to (4) is introduced, the chemical step being defined by k. When the $EC_{2X}E$ reaction is only limited by the concentration of B, the problem can be described using an ECE formulation, assuming a large excess of the species X and considering the relationship (5) between k and K'. The reactions 1 and 4 are assumed to be rapid and only limited by diffusion.

Moreover, two kinetic constants are introduced for every redox reaction 1 and 4 in order to impose its direction, i.e., oxidation or reduction, at the microelectrode.

$$A \underset{k_{red1}}{\overset{k_{ox1}}{\rightleftharpoons}} B \tag{6}$$

$$C \underset{k_{red2}}{\overset{k_{ox2}}{\rightleftharpoons}} E \tag{7}$$

where k_{ox1}, k_{red1}, k_{ox2}, and k_{red2} represent the respective rate constants of the oxidation and reduction of reactions 6 and 7. The complete mechanisms are schematically described in Figure 2. The ratio k_{oxi}/k_{redi} is maintained at 1000 in order to establish an oxidation regime at the electrode.

In the present model, the convection diffusion of the five species is studied in a steady-state regime in a 2D cross section of the geometry (see eq 8). The migration effects are neglected.

$$\frac{\partial c_i}{\partial t} + \text{div}(-D_i \nabla c_i) + \mathbf{V} \cdot \nabla c_i = R_i \tag{8}$$

where c_i is the concentration of the species i, D_i its diffusion coefficient, $\mathbf{V}$ is the fluid velocity vector, and R_i is the rate of generation or consumption of the species i. The consumption and production of the different species in the domain (R_i) is implemented in the differential equation system, following the kinetics of reactions 1−7. The details of the finite element integral formulation of the problem are described in Appendix 1.

The 2D geometry used in the model, assuming $w/2h \gg 1$ to neglect the velocity gradient in the third space direction (z axis), is far from the experimental dimension ($w/2h = 1$). However, it allows a first approach of the different phenomena involved in the present problem. Besides, the solution is supposed to be sufficiently diluted to ensure a uniform viscosity and density of the fluid, whatever the concentration gradients are. The channel walls are assumed to be smooth, and the wall capillary forces are neglected. Finally, diffusion coefficients are assumed to be uniform in the entire domain, and thermal effects are neglected.

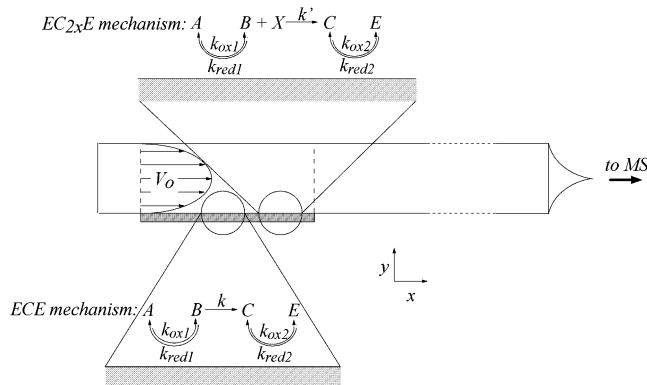**Figure 1.** Schematic representation of the channel electrode geometry.

Figure 2. Scheme of the model including illustrations of the ECE and EC$_{2X}$E mechanisms.

The present model is based on a microband channel electrode, where x_e, d, and h are defined as electrode length, channel depth, and channel half-height, respectively, as illustrated in Figure 1. Referring to Figure 1 and Figure 2, we can define the following dimensionless parameters,

$$Q = \frac{4dhV_0}{3} \qquad p_1 = \frac{x_e}{h} \qquad p_2 = \frac{Q}{dD} \qquad (9)$$

where Q is the volume flow rate defining the laminar flow conditions and V_0 is the maximum fluid velocity of the corresponding fully developed Poiseuille flow profile. Several dimensionless parameters are also introduced, as described in the literature.[35] The shear rate Peclet number P_S indicates the relative importance of convection compared to diffusion. The dimensionless reaction rate and rate constant of the global ECE mechanism are given by K_{ECE} and K, respectively.

$$P_s = \frac{3}{2}p_1{}^2 p_2 \qquad (10)$$

$$K_{ECE} = \frac{kx_e{}^2}{D} \qquad (11)$$

$$K = P_s{}^{-2/3} K_{ECE} \qquad (12)$$

$$N_{eff} = I_K / I_0 \qquad (13)$$

N_{eff} is defined as the effective number of electrons transferred during the whole ECE (or EC$_{2X}$E) process normalized by the initial E step. I_K is the current provided by the whole ECE (or EC$_{2X}$E) mechanism while I_0 is the current consumed for the first step

(35) Compton, R. G.; Page, D. J.; Sealy, G. R. *J. Electroanal. Chem.* **1984**, *161*, 129−145.

(1), assuming a one-electron process for every electrochemical reaction. The current corresponding to the second electrochemical reaction 4 depends on the production of the species C. If the flow rate is high and the rate constant of the chemical step is low, the generation of C will be low, giving rise to low oxidation current. In this case, N_{eff} will be close to 1 (i.e., close to a one-electron behavior) due to the almost complete inhibition of reaction 4. Conversely, if the flow rate is low and the kinetics of the homogeneous reaction fast, C will be produced in large quantities leading to an overall two-electron process (N_{eff} = 2). The convection and the kinetic conditions are related to P_S and K, respectively.

To study the steady state of the on-line tagging, the transversal mean concentration of every species involved in the EC$_{2X}$E process is calculated at a defined x position according to

$$<c_i(x)> = \frac{1}{2h}\int_0^{2h} c_i(x)\,y \qquad (14)$$

NUMERICAL DESCRIPTION

The finite element software Flux-Expert (Simulog)[36] is operated on a Silicon Graphics Octane 2 Unix workstation. The model is formulated in a 2-D Cartesian form (see Appendix 1) and calculations are based on FEM, which have been reported to extend the kinetic range for ECE and similar mechanisms.[37] Nonlinear algorithms based on the Gauss inversion method are used for all the calculations. The iterative scheme is performed with a precision criterion of 1% for the convergence. A steady-state algorithm is applied in most of the cases, while a transient is chosen for low concentrations of species X on short electrode geometries. For this last case, the fulfillment of the steady state is verified with a typical duration of 0.4 s, with nine time steps from 0.02 to 0.1 s (case of the short electrode calculations). Thanks to the nonlinearity iterations, the mesh can be enlarged, corresponding to a more than 3-fold decrease in the number of nodes (an error of −0.15% compared to the thinner mesh is obtained, while this error is −5.4% with the static algorithm).

To avoid a boundary condition conflict at the interfaces between the electrode and insulated walls concerning the flux directions, a slightly recessed geometry is used.[38] The recess size ranges from 0.1% to 0.3% depending on the electrode length. Its influence on the calculation precision is detailed in Appendix 2. The boundary conditions used are defined below.

$$\frac{\partial c_A}{\partial n} = \frac{\partial c_B}{\partial n} = \frac{\partial c_C}{\partial n} = \frac{\partial c_E}{\partial n} = 0, \quad \text{for } y = 0, x < 0, \text{ and } x > x_e$$

$$\frac{\partial c_A}{\partial n} = \frac{\partial c_B}{\partial n} = \frac{\partial c_C}{\partial n} = \frac{\partial c_E}{\partial n} = 0, \quad \text{for } y = 2h, \forall x \qquad (15)$$

$$c_A = c_A^0, \; c_X = c_X^0, \; c_B = c_C = c_E = 0, \quad \text{for } 0 < y < 2h, x = -l$$

where l is the distance between the cell inlet and the origin (electrode leading edge) as defined in Figure 1. Furthermore, the following conditions for the consumption or production of species
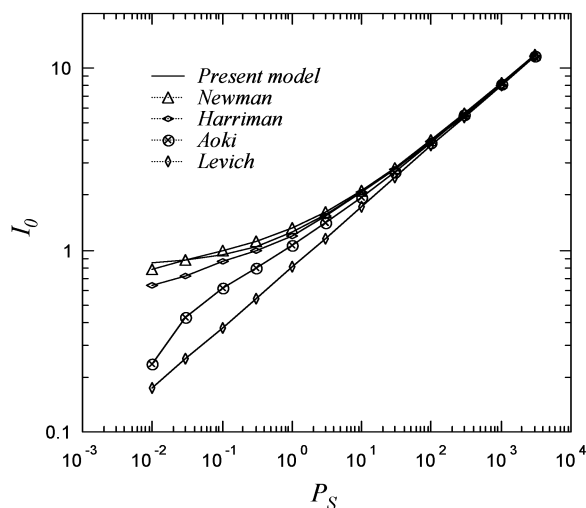
Figure 3. Comparison of the analytical and simulated values of the current I_0 for a range of P_S for a short electrode: Levich,[43] Newman,[40] and the Aoki group[47] calculated values according respectively to eqs 18–20 (see Appendix 2); simulated values of Harriman et al.[39] ($x_e = 5\ \mu$m, $V_0 = 0.5$ m·s^{-1}, $h = 200\ \mu$m; $c_A^0 = 1$ mM; $D_A = 1 \times 10^{-9}$).

at the electrode are fulfilled according to the kinetic constants introduced in eqs 6 and 7.

$$\frac{\partial c_A}{\partial n} = k_{ox1} c_A = -\frac{\partial c_B}{\partial n} = -k_{red1} c_B$$

$$\frac{\partial c_C}{\partial n} = k_{ox1} c_C = -\frac{\partial c_E}{\partial n} = -k_{red2} c_E \qquad (16)$$

For the transient calculations, the initial conditions are the following:

$$c_A = c_A^0,\ c_X = c_X^0,\ c_B = c_C = c_E = 0 \qquad (17)$$

RESULTS AND DISCUSSION

Model Validation. The mesh parameters, i.e., recess size and electrode mesh, are validated according to literature values[39] with an error of 0.2% (see Appendix 2, Short Electrode Validation), based on an E mechanism.

The model is also evaluated according to P_S values (corresponding to the convection effect). As shown in Figure 3, the values obtained are in good agreement with the literature, except for low P_S values, for which the current is slightly overestimated. For high P_S values, a good agreement is, however, found with an analytical model put forward by Newman and co-workers.[40]

The model is also evaluated regarding ECE and EC$_{2X}$E mechanisms. For this purpose, a comparison is made with

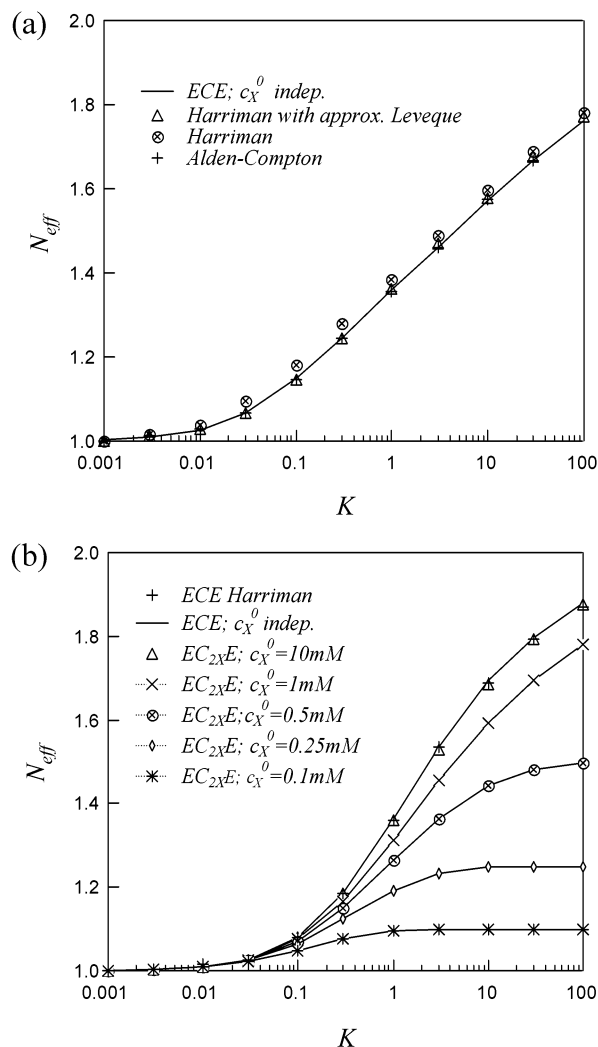(36) Simulog: 35 Chemin du Vieux Chene 38240 Meylan Zirst–France; anne-marie.bernier@simulog.fr.

(37) Stevens, N. P. C.; Gooch, K. A.; Fisher, A. C. *J. Phys. Chem. B* **2000**, *104*, 1241–1248.

(38) Ferrigno, R.; Brevet, P. F.; Girault, H. H. *Electrochim. Acta* **1997**, *42*, 1895–1903.

(39) Harriman, K.; Gavaghan, D. J.; Houston, P.; Suli, E. *Electrochem. Commun.* **2000**, *2*, 567–575.

(40) Newman, J. In *Electroanalytical Chemistry*; Bard, A. J., Ed.; Marcel Dekker: New York, 1973; Vol. 6, pp 187–373.

Figure 4. Working curves for an ECE mechanism at a short electrode ($x_e = 5\ \mu$m, $V_0 = 0.5$ m·s^{-1}, $h = 200\ \mu$m; $c_A^0 = 1$ mM; $c_X^0 = 10$ mM; $D_i = 1 \times 10^{-9}$) at low flow rate, log $P_S = -2.4$ (a), for an ECE and an EC$_{2X}$E mechanism at medium flow rate, log $P_S = 0$ (b); Dotted curves represent the effect of the depletion of X on N_{eff}.

previous works.[41,42] The effective transfer of electrons N_{eff} is calculated for two flow rates. The working curves are obtained in the following cases by varying the kinetic constants k (ECE mechanism) or k' (EC$_{2X}$E mechanism). As illustrated in Figure 4a, the simulated results for low flow rate are very close to those of Alden and Compton,[42] as well as those of Harriman et al.[41] with Leveque approximation. At higher flow rate (log $P_S = 0$), the results displayed in Figure 4b are in very good agreement with the values of ref 41. In this case, the two mechanisms, ECE and EC$_{2X}$E, are considered in order to assess the second set of equations. The ECE mechanism is indeed an asymptotic case of EC$_{2X}$E where $c_X^0/c_A^0 \gg 1$; i.e., c_X^0 do not affect the whole reaction. To calibrate the EC$_{2X}$E model on the ECE situation, an excess of X ($c_X^0 = 10$ mM) and relation 5 are taken into account. The errors between the two sets of results remain within -0.25%.

Figure 4b permits a quantification of the effect of the depletion of X on the EC$_{2X}$E phenomenon, displaying the working curves

(41) Harriman, K.; Gavaghan, D. J.; Houston, P.; Kay, D.; Suli, E. *Electrochem. Commun.* **2000**, *2*, 576–585.

(42) Alden, J. A.; Compton, R. G. *J. Phys. Chem. B* **1997**, *101*, 9741–9750.

calculated for c_X^0 ranging from 0.1 to 10 mM. For $c_X^0 < 1$ mM, the convergence of the model could not be reached with the last set of equations. Therefore, a nonlinear dynamic (transient) algorithm with 0.4-s duration is also chosen. Referring to Figure 4b, the depletion of X is found to have a tremendous effect on the EC$_{2X}$E mechanism. At low K values, reaction 4 is kinetically limited and the effect of c_X^0 is insignificant in contrast to the situation at high K values. Thus, X is totally consumed near the electrode, and consequently, the generation of C and E is strongly limited, leading to the plateau characterizing the limit of diffusion control.[43]

After these initial validations, a new mesh is generated to simulate our system. The mesh is then optimized according to the same parameters as introduced above. The reference case is calculated using the following values: $x_e = 100\ \mu$m, $V_0 = 4$ mm·s^{-1}, $h = 20\ \mu$m, $L = 400\ \mu$m, recess size 0.03 μm, recess mesh 0.01 μm, and electrode mesh size 1.225 μm (see Appendix 2 for the Long Electrode Validation).

Model Assessment According to the Experimental Case. For the EC$_{2X}$E mechanism studies, the goal is usually to get the highest value for N_{eff}, because the amperometric detection of the adduct is based on the second electrochemical step (4). The purpose here is to optimize the yield of the adduct formation, in both reduced (C) and oxidized (E) states. Since both forms can be detected by MS, the ratio $(c_C + c_E)/c_X^0$ will therefore be considered throughout this study. For all the calculations presented below, the P_S value is kept constant ($P_S = 4000$; log $P_S =$ 3.6) corresponding to a high flow rate regime. For this geometry, the corresponding velocity is one of the lowest that can be used in an actual experiment. Indeed, below a certain flow rate (150 nL·min^{-1}), it becomes difficult to obtain an efficient and stable nanospray, which is of utmost importance for MS analysis.

The present model is evaluated by considering the experimental conditions used for the electrochemically induced tagging of proteins in the present nanospray.[30] For this purpose, the ratio c_A^0/c_X^0 is set to 10^3, the channel length is extended to $L = 7.9 \times 10^{-3}$ m, and the rate constant K is equal to the one determined for the addition of cysteine to protonated benzoquinone ($K = 0.21$ mM^{-1}·s^{-1}).[34] The depletion of X implies that the second electrochemical step is largely inhibited compared with the first one, and so, N_{eff} remains close to 1 even for relative high K values (for $K = 10^4$ mM^{-1}·s^{-1}, $K = 397$). Furthermore, due to the large size of the electrode, a static algorithm is found to converge, despite the low values of c_X^0. The diffusion coefficients are assumed to be equal for all the species ($D_i = 1 \times 10^{-9}$ m^2·s^{-1}). It will be demonstrated in the next section that the diffusion coefficient of the target does not affect the tagging yield significantly.

As illustrated in Figure 5, the tagging for relatively low rate constants is still efficient if a sufficiently long channel is used. Considering an electroosmotic flow (EOF) profile ($V_0/V_{\text{mean}} = 1$), 65% of the target species are tagged versus 52% in the case of a pressure-driven flow (PDF) profile ($V_0/V_{\text{mean}} = 1.5$). This result points out the influence of the flow profile on the final tagging efficiency. Referring to the experimental case,[30] a final yield of 30% is expected. This difference can be explained by considering the 3-D geometry effects on the experimental flow profile. The
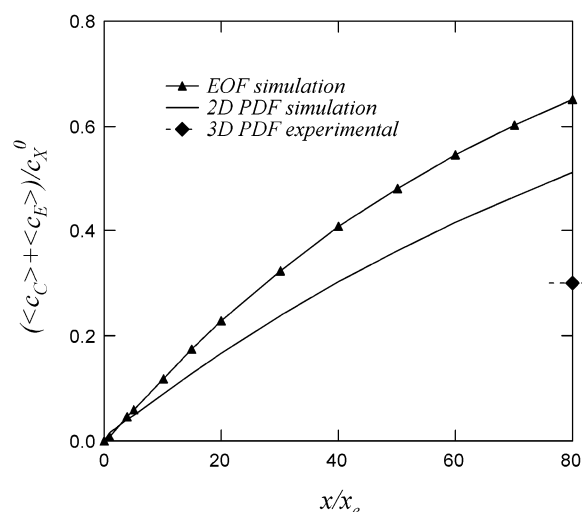
(43) Levich, V. G. *Physicochemical Hydrodynamics*, 2nd ed.; Prentice-Hall: Englwood Cliffs, NJ, 1962.

**Figure 5.** Distribution of the mean concentration of the total adduct amount along the x axis in the experimental conditions described in refs 30 and 34 ($c_A^0/c_X^0 = 10^3$, $K = 0.21$ mM^{-1}·s^{-1}, $L = 7.9 \times 10^{-3}$ m). Comparison between EOF and PDF for the same flow rate ($V_0^{\text{EOF}} = 2.67 \times 10^{-3}$ m·s^{-1}, $V_0^{\text{PDF}} = 4 \times 10^{-3}$ m·s^{-1}, $x_e = 100\ \mu$m, $h = 20\ \mu$m; $c_A^0 = 10$ mM; $c_X^0 = 0.01$ mM; $D_i = 1 \times 10^{-9}$ m^2·s^{-1}).

channel geometry in the photoablated microstructures has a trapezoidal cross section with a $w/2h$ ratio close to 1. The resulting PDF profile is thus warped and characterized by a higher V_0/V_{mean} ratio. Relative to the two parallel plates (present model), the other asymptotic case of the geometry is the tube, which is defined by $V_0/V_{\text{mean}} = 2$. However, the axisymmetric geometry would imply a ring electrode, which is not compatible with the present situation. The effect of the flow profile is investigated in detail in the next section, to highlight and characterize the different phenomena involved in the tagging process. According to Figure 5, the 2-D calculations considering PDF and EOF profiles allow the extrapolation of the experimental final tagging efficiency. Nevertheless, a 3-D simulation study could give a more accurate evaluation of the latter.

Description of the Phenomena. To make possible comparison with the experimental case,[34] the ratio c_A^0/c_X^0 is chosen to be 0.01. Furthermore, a shorter channel length is taken into account ($L = 400\ \mu$m), to focus on the phenomena involved in the surroundings of the electrode, i.e., the area where all the reactions of the EC$_{2X}$E occur. This approach is also relevant for the experimental situation where the adducts are not stable and need to be analyzed by MS immediately after their generation.

First, the case of a specific rate constant is studied. As illustrated by the isovalues presented in Figure 6a and b, a homogeneous reaction having a rate constant of $K = 10^3$ mM^{-1}·s^{-1} ensures the complete consumption of X at the end of the channel and consequently the maximum production of C. Concurrently, there is a huge depletion of the latter species at the electrode due to the second electrochemical step (reaction 4). Figure 6c shows the resulting localized distribution of E at the electrode. It is worth noticing that the concentration of C exceeds that of E at the end of the channel, since the production zone for E is confined to the microelectrode surroundings, while C is produced in the entire channel.
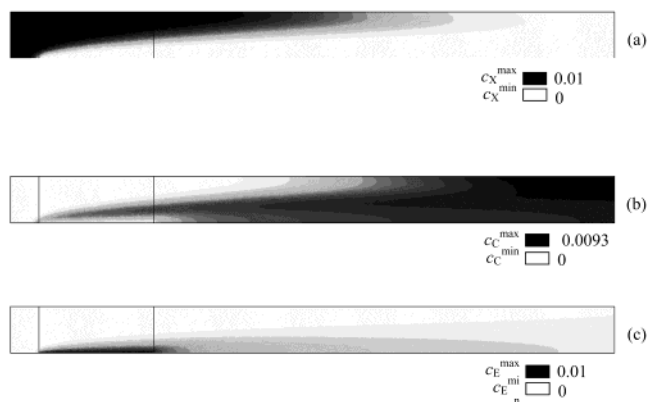
Figure 6. Isovalues of c_X (a), c_C (b), and c_E (c) for $K = 10^3$ mM^{-1}·s^{-1} ($x_e = 100$ μm, $V_0 = 4 \times 10^{-3}$ m·s^{-1}, $h = 20$ μm; $c_A^0 = 1$ mM; $c_X^0 = 0.01$ mM; $D_i = 1 \times 10^{-9}$ m^2·s^{-1}).
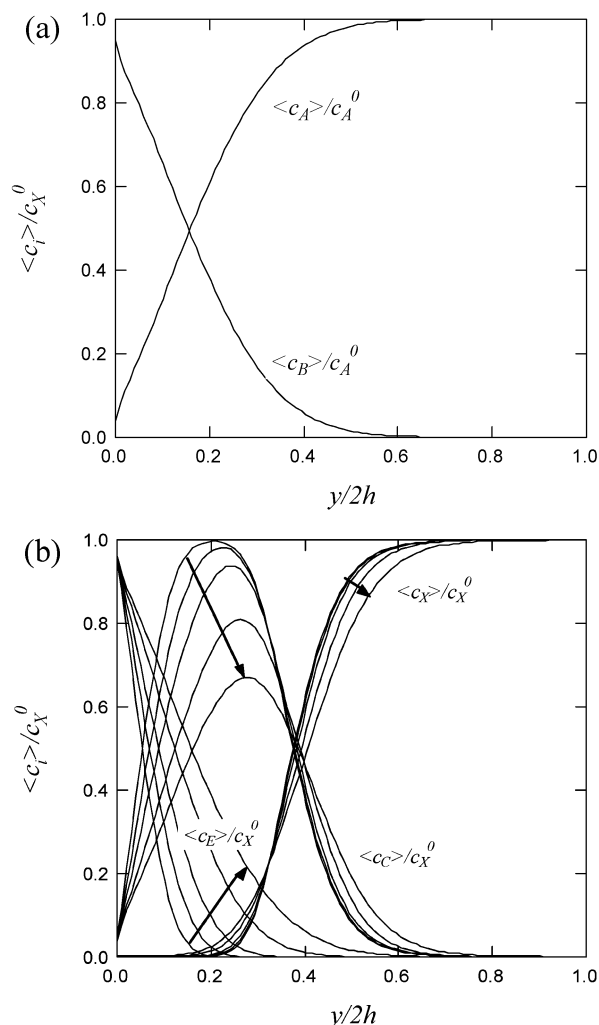

Figure 7. Transversal concentration profiles of species A and B (a) and X, C, and E (b) at the end of the electrode ($x/x_e = 1$) at different diffusion coefficients: $D = 5 \times 10^{-11}$, 1×10^{-10}, 2×10^{-10}, 5×10^{-10}, and 1×10^{-9} m^2·s^{-1} ($K = 10^3$ mM^{-1}·s^{-1}, $x_e = 100$ μm, $V_0 = 4 \times 10^{-3}$ m·s^{-1}, $h = 20$ μm; $c_A^0 = 1$ mM; $c_X^0 = 0.01$ mM).

In Figure 7 are shown the relative concentration profiles along the y axis of the five species at the end of the electrode considering a rate constant $K = 10^3$ mM^{-1}·s^{-1}. For $y/2h < 0.15$, half of the total amount of A is consumed, but it can be noted that c_A remains unchanged for $y/2h > 0.5$. In other words, the consumption of A

Table 1. Effect of the Diffusion Coefficient on the Transversal Mean Concentration and Yield at the Channel Outlet[a]

	D/m^2·s^{-1}	
	1×10^{-9}	5×10^{-11}
$<c_X>/c_X^0$	0.007	0.014
$<c_C>/c_X^0$	0.878	0.958
$<c_E>/c_X^0$	0.114	0.028
$(<c_C> + <c_E>)/c_X^0$	0.992	0.986

[a] Values: ($x/x_e = 5$) ($K = 10^3$ mM^{-1}·s^{-1}, $x_e = 100$ μm, $V_0 = 4 \times 10^{-3}$ m·s^{-1}, $h = 20$ μm; $c_A^0 = 1$ mM; $c_X^0 = 0.01$ mM).

is not optimized. However, the residence time cannot be extended experimentally by a diminution of the velocity value, as already mentioned above. As illustrated in Figure 7a, a smaller channel height would thus be more appropriate, to increase the probability of B and X to react.

As expected, the same depletion zone is found for X (see Figure 7b). Due to the EC$_{2X}$E process, a part of the adduct C undergoes an oxidation, thereby producing the species E. This effect is particularly observed in the solution surrounding the electrode ($y/2h \leq 0.25$). For $y/2h > 0.7$, the initial concentrations remain unchanged. This distribution suggests that h is optimized when an X depletion is observed along the entire channel depth.

When the nature of the targets for an electrochemically induced tagging, such as amino acids, peptides, and proteins, are considered, the diffusion coefficients are considerably different. Therefore, this effect is studied by using lower diffusion coefficient values for the target X as well as the two adducts C and E (down to $D = 5 \times 10^{-11}$ m^2·s^{-1}, which corresponds to the diffusion coefficient of myoglobin, 17 kDa[44]).The mesh is also refined to keep the Peclet mesh number sufficiently low to ensure that the error is less than 0.01% (mesh size 3 μm; Reynolds mesh number 0.03; Peclet mesh number 12 with $D = 1 \times 10^{-9}$ m^2·s^{-1}; i.e., for A and B species, the Peclet mesh number is 240 with $D = 5 \times 10^{-11}$ m^2·s^{-1}, for X, C, and E species). For a mixing situation, the critical value of the Peclet mesh number is $\sim$100.[45]

As illustrated by the transversal concentration profiles displayed in Figure 7, the diminution of the diffusion coefficient of the target induces a more accentuated confinement for the latter as well as for the tagged species. The concentration profiles of the adducts C and E are thus shifted to the lower part of the channel, while the limit of consumption of X is more abrupt. The flux of C to feed the electrode reaction is reduced, resulting in an increase in its local concentration. As pointed out by the unchanged profiles in Figure 7a, the decrease of the diffusion coefficient of the target does not affect the concentration of the species A and B, due to their high relative concentration value ($c_{A,B}/c_X^0 = 100$).

Considering the effect of the diffusion coefficient on the mean transversal concentration of X, C, and E at the channel outlet ($x/x_e = 5$), it is worth noticing that the X consumption is relatively unaffected, as well as the total adduct amount (see Table 1). It

(44) Vesterberg, O.; Svensson, H. *Acta Chem. Scand.* **1966**, *20*, 820.
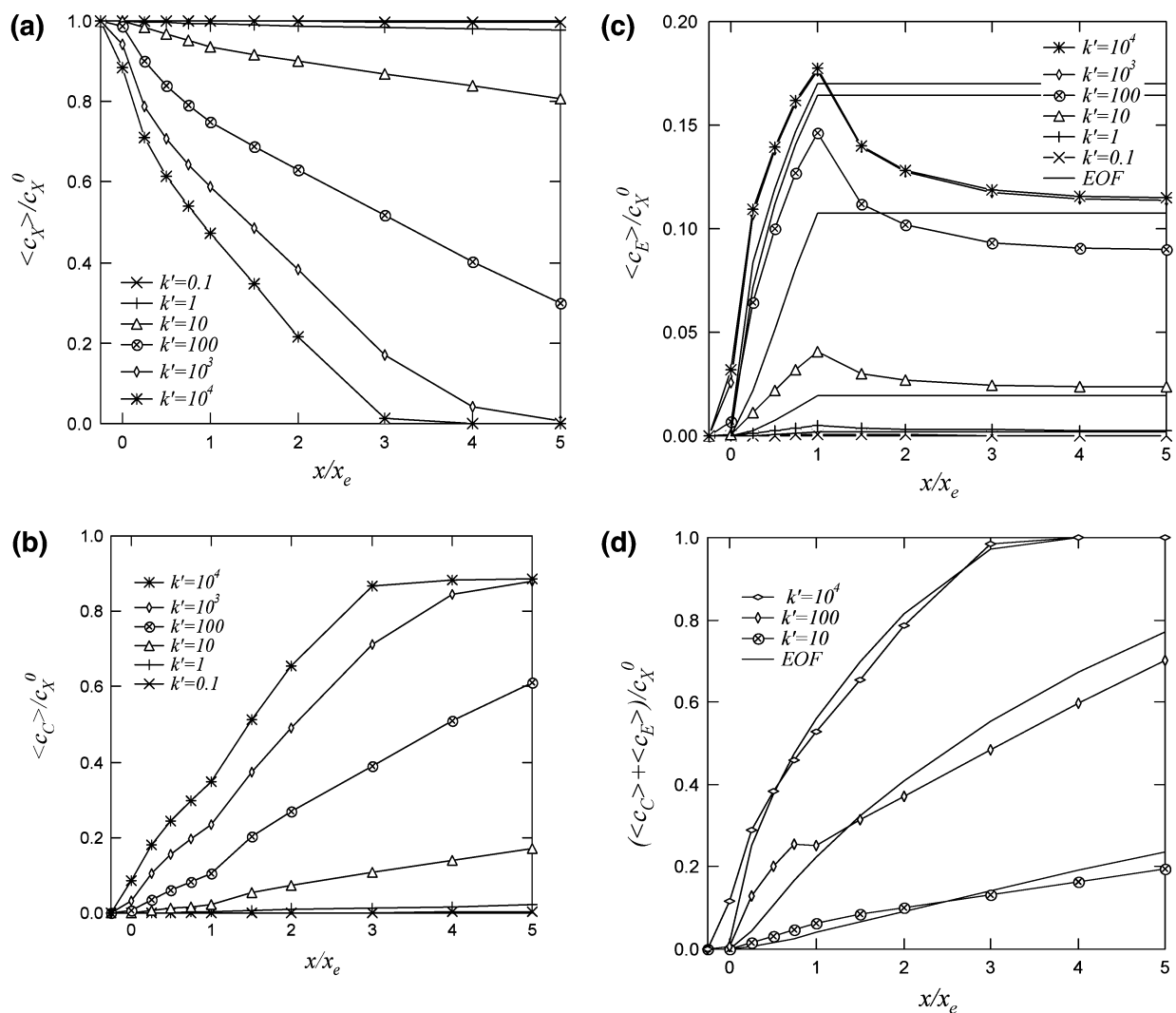(45) Mengeaud, V.; Josserand, J.; Girault, H. H. *Anal. Chem.* **2002**, *74*, 4279–4286.

Figure 8. Distribution of the mean concentration of X (a), C (b), and E (c) and of the total amount of adduct (d) along the x axis at different values of rate constant k' according to eq 14. Comparison between EOF and PDF for the same flow rate ($V_0^{EOF} = 2.67 \times 10^{-3}$ m·s⁻¹, $V_0^{PDF} = 4 \times 10^{-3}$ m·s⁻¹, $x_e = 100$ μm, $h = 20$ μm; $c_A^0 = 1$ mM; $c_X^0 = 0.01$ mM; $D_i = 1 \times 10^{-9}$ m²·s⁻¹).

can be explained by the fact that the initial concentration of X is uniform: its contribution to the tagging reaction is not limited by a boundary layer diffusion and is therefore independent of its diffusion coefficient. Its decrease favors C to the detriment of E. In the framework of the on-line tagging in the nanospray, these results show that the modification yield is not affected by the size of the targets (amino acids, peptides, proteins). As shown by this table, the second electrochemical reaction is negligible. As a consequence, the faradaic current generated during the spray process is totally dedicated to the electrogeneration of B. Furthermore, the current involved in the oxidation of the adduct is almost equal to zero. As the nanospray works as a controlled-current electrolytic cell,[46] the concentration of the latter can be easily calculated.[28]

Kinetic and Convective Aspects of the Tagging. The transversal mean concentrations of the five species are calculated at different positions along the channel (x axis) according to eq 14. These profiles are determined for different rate constants k'. The effect of the latter on the concentrations of X, C, and E is

illustrated in Figure 8a–c, respectively. As displayed in Figure 8a, a value of $k' = 10^3$ mM⁻¹·s⁻¹ is needed for this geometry and flowing condition to obtain a complete consumption of X. In Figure 8b, one can also see the slope increase for the C concentration immediately after the end of the electrode. This fact is easily understood since it is not consumed far from the electrode (reaction) as already illustrated in Figure 7b. In Figure 8c, the limit of the electrochemical production is undoubtedly identified at $x/x_e = 1$, but downstream the E concentration drops and does not remain stable as expected (conservation of E in the region where it does not undergo any reaction). This phenomenon is caused by the parabolic profile of the pressure-driven flow (PDF), since the fluid velocity value is very low at the edges of the channel. The concentrated zone of E, surrounding the electrode, moves much slower than the center of the flow, resulting in a pseudoaccumulation of E at the electrode and in a dilution effect after the microelectrode. The last effect is due to the high velocity of the arriving central part of the flow, which is free from E species. This assumption is confirmed by a calculation based on an EOF regime, assuming a flat velocity profile. As illustrated in Figure

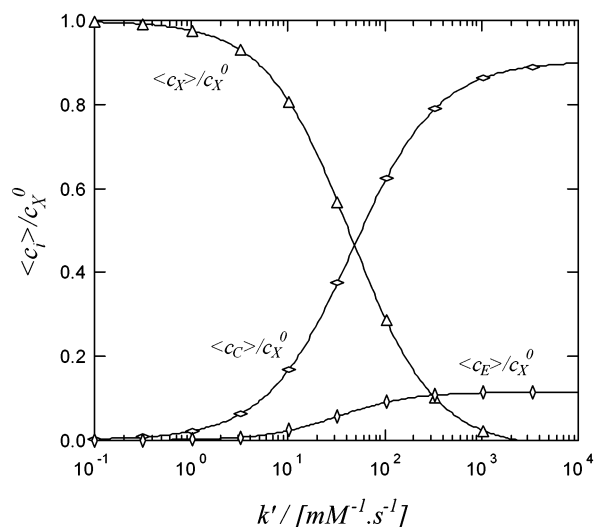(46) Van Berkel, G. J.; Zhou, F. *Anal. Chem.* **1995**, *67*, 2916–2923.

Figure 9. Mean concentration of X, C, and E at the end of the channel ($x/x_e = 5$) versus the rate constant k' ($x_e = 100$ μm, $V_0 = 4 \times 10^{-3}$ m·s^{-1}, $h = 20$ μm; $c_A^0 = 1$ mM; $c_X^0 = 0.01$ mM; $D_i = 1 \times 10^{-9}$ m^2·s^{-1}).

8c, the concentration of E remains at its maximum downstream from the electrode, regardless of the rate constant. Nevertheless, the differences between the E concentration profiles obtained with PDF and EOF flows need to be unraveled. At low k' values ($k' < 100$), the pressure flow favors the oxidation of C at the electrode over the EOF, due to the longer residence time at the electrode. When the homogeneous kinetic is faster, the influence of the residence time is damped by the depletion of X. Consequently, the postelectrode dilution effect is not compensated by the increase in the residence time near the electrode. As shown in Figure 8d, the yield of the modification, defined above as ($c_C + c_E)/c_X^0$, confirms the result previously described for the flow profile on the EC$_2$XE mechanism (illustrated for $k' = 100$ mM^{-1}·s^{-1}). For $x < x_e$, B is confined to the electrode surroundings. Therefore, the production of C and E is favored in the same region, due to an increased residence time. When $x > x_e$, the unreacted B molecules diffuse toward the center of the channel and are then transported rapidly to the outlet by convection. Therefore, the time to react with X is globally reduced compared to the EOF case. This is illustrated in Figure 8d, where it can be observed that the PDF yield is lower than the EOF yield for $x > x_e$.

The influence of k' on the C and E concentration profiles is not linearly progressive, as observed in Figure 8c. The range $k' = 10-100$ mM^{-1}·s^{-1} defines indeed a border at which reaction 4 dominates. This corresponds to the values $K = 0.397 - K = 3.97$, i.e., the same range for which the largest increase of N_{eff} is observed at equivalent flow rate (see Figure 4b). This strong increase between $k' = 10$ mM^{-1}·s^{-1} and $k' = 100$ mM^{-1}·s^{-1} is also observed on the total adduct production (see Figure 8d). To reach or exceed this "threshold" value of rate constant, one possibility is to use different probes. Indeed, experimental values of k' have already been determined in the case of the tagging of cysteines with quinonoid compounds. Roussel et al. obtained $k' = 0.21$ mM^{-1}·s^{-1} for the reaction of the cysteine with electrogenerated benzoquinone,[34] while Brookes and co-workers determined $k' = 125$ mM^{-1}·s^{-1} with acetamidophenol,[33] indicating a wide range of rate constants for this kind of compound.

The mean concentration evolution versus k' of the species X, C, and E is displayed in Figure 9 for $x/x_e = 5$ (end of the channel). The value of k', for which the half-modification is obtained, can thus be determined. As expected, this value ($k_{1/2}' = 42$ mM^{-1}·s^{-1}) is within the range defined above; i.e., $k' = 10-100$ mM^{-1}·s^{-1}. Furthermore, in the present model, a 90% modification requires a rate constant $k_{\text{opt}}' = 330$ mM^{-1}·s^{-1}. For a given geometry, this representation allows a quantification of the global tagging efficiency for different probe−target couples.

CONCLUSIONS

In this study, a numerical model of the electrochemically induced EC$_2$XE tagging in a nanospray channel has been developed. The effect of the depletion in the target is shown to be drastic regarding the electrode current ratio N_{eff}. Furthermore, the kinetic aspects of the tagging have been investigated and the different phenomena involved in the EC$_2$XE mechanism have been pointed out. It has been shown that the flow profile can modify the yield distribution along the channel due to changes in the residence time at different transversal locations. This effect is particularly marked for low rate constant on-line tagging.

To increase the yield of the electrochemical tagging regardless of the kinetic aspect, several alternative geometries could be considered, such as a metallic foil wedged between two plastic substrates having flow channels. In this way, the electrode surface would thus be doubled and the electrogenerated species could diffuse from both sides into the bulk.

It has also been demonstrated that the efficiency of this on-line reaction can be assessed for a specific probe−target system by considering the geometry and flowing conditions. In the framework of a quantitative proteomics analysis, such as the ICAT technology, two electroactive probes can be chosen to tag specifically two cell states. To infuse the different mixtures, a nanospray interface design could consist in a Y junction channel mixing downstream of these two sets of on-line tagged proteins before the interface outlet. In this context, the present model allows an optimization of the conditions needed to obtain a full tagging of the two protein mixtures before mixing.

APPENDIX 1

The general eq 8 can be detailed as following, by taking into account the diffusion−convection reaction equations for the five considered species. To simplify the writing, the Nabla notation is used.

$$\frac{\partial c_A}{\partial t} + \nabla \cdot (-D_A \nabla c_A + \mathbf{V} c_A) = -k_{\text{ox1}} c_A + k_{\text{red1}} c_B \quad \text{(A.1)}$$

$$\frac{\partial c_B}{\partial t} + \nabla \cdot (-D_B \nabla c_B + \mathbf{V} c_B) = +k_{\text{ox1}} c_A - k_{\text{red1}} c_B - k' c_B c_X \quad \text{(A.2)}$$

$$\frac{\partial c_X}{\partial t} + \nabla\cdot(-D_X\nabla c_X + \mathbf{V}c_X) = -K'c_B c_X \quad (A.3)$$

$$\frac{\partial c_C}{\partial t} + \nabla\cdot(-D_C\nabla c_C + \mathbf{V}c_C) = -k_{ox2}c_C + k_{red2}c_E + K'c_B c_X \quad (A.4)$$

$$\frac{\partial c_E}{\partial t} + \nabla\cdot(-D_E\nabla c_E + \mathbf{V}c_E) = -k_{ox2}c_C + k_{red2}c_E \quad (A.5)$$

where k_{ox1}, k_{ox2}, k_{red1}, and k_{red2} are defined on the electrode surface only, K' being defined on all the domain. These expressions are derived in the global general form (A.8), using the Galerkin's formulation (multiplication by a second-order projective function α and integration on the domain of study, Ω).

$$\int\int_\Omega \alpha\left[\frac{\partial c_i}{\partial t} + \nabla\cdot(-D_i\nabla c_i + \mathbf{V}c_i) \pm k_{ox,red}c_{i,j} \pm K'c_i c_k\right]d\Omega = 0 \quad (A.6)$$

The convection term is derived by taking into account the continuity equation $\nabla\cdot\mathbf{V} = 0$. By decomposing the product between α and the divergence, the second-order derivative of (A.6) (divergence of the gradient) becomes

$$\alpha\nabla\cdot(-D_i\nabla c_i) = \nabla\cdot(-\alpha D_i\nabla c_i) + D_i\nabla\alpha\cdot\nabla c_i \quad (A.7)$$

Applying (A.7) in (A.6) and using the Ostrogradsky theorem, the divergence term is rejected at the boundary (A.8), where it expresses the flux conditions of the species i. In the present case, this boundary condition is equal to zero (no flux at the boundaries of the domain).

$$\int\int_\Omega \alpha\left[\frac{\partial c_i}{\partial t} + D_i\nabla\cdot\alpha\nabla c_i + \alpha\mathbf{V}\cdot\nabla c_i \pm \alpha k_{ox,red}c_{i,j} \pm \right.$$
$$\left. \alpha K'c_i c_k\right]d\Omega = \int_{\partial\Omega}\alpha D_i\frac{\partial c_i}{\partial n}\,d\mathbf{l} = 0 \quad (A.8)$$

Equation A.8 is applied to the initial set (A.1–A.5), which is expressed in a matricial form. The steady-state part of this matrix (local form for a given node) is described in (A.9), where β is the interpolation function of the unknown vector $[c_A\ c_B\ c_X\ c_C\ c_E]$ (second-order polynomial function):

$D_A\nabla\alpha\cdot\nabla\beta+$ $\alpha\mathbf{V}\cdot\nabla\beta+$ $\alpha k_{ox1}\beta$	$-\alpha k_{red1}\beta$			
$-\alpha k_{ox1}\beta$	$D_B\nabla\alpha\cdot\nabla\beta+$ $\alpha\mathbf{V}\cdot\nabla\beta+$ $\alpha k_{red1}\beta+$ $\alpha k'\beta c_X$	$\alpha k'\beta c_B$		
		$D_X\nabla\alpha\cdot\nabla\beta+$ $\alpha\mathbf{V}\cdot\nabla\beta+$ $\alpha k'\beta c_B$		
		$-\alpha k'\beta c_B$	$D_C\nabla\alpha\cdot\nabla\beta+$ $\alpha\mathbf{V}\cdot\nabla\beta+$ $\alpha k_{ox2}\beta$	$-\alpha k_{red2}\beta$
			$-\alpha k_{ox2}\beta$	$D_E\nabla\alpha\cdot\nabla\beta+$ $\alpha\mathbf{V}\cdot\nabla\beta+$ $\alpha k_{red2}\beta$

(A.9)

Table 2. I_0 Current Values[a] Compared with Simulated Result[39] and Analytical Approximations[40,43,47]

	$I_0/(-)$	error/%
simulated value	6.59820	
Harriman[39]	6.599555	−0.021
Levich[43]	6.409131	2.950
Newman[40]	6.634661	−0.550
Aoki[47]	6.545923	0.799

[a] Values: $x_e = 10\ \mu m$, $V_0 = 0.5\ m\cdot s^{-1}$, $h = 200\ \mu m$; recess size, 0.03 μm; recess mesh, 0.01 μm; electrode mesh, 80; $c_A^0 = 1$ mM.

Table 3. Effect of the Recess Size r and the Recess Mesh Size m on the Current Value I_0 for a Small Electrode[a]

$r/\mu m$	$m/\mu m$	$I_0/(-)$
0.03	0.01	6.59820
0.03	0.03	−0.17%
0.1	0.03	−2.55%
0.1	0.1	−2.61%

[a] Values: $x_e = 10\ \mu m$, $V_0 = 0.5\ m\cdot s^{-1}$, $h = 200\ \mu m$; electrode mesh, 80; $c_A^0 = 1$ mM.

Table 4. Effect of the Electrode Mesh on the Current Value I_0 for a Small Electrode[a]

mesh number	$I_0/(-)$	error/%
80 (0.1 μm)	6.59820	
40 (0.2 μm)	6.60093	0.04
30 (0.27 μm)	6.60390	0.09
20 (0.4 μm)	6.61322	0.23

[a] Values: $x_e = 10\ \mu m$, $V_O = 0.5\ m\cdot s^{-1}$, $h = 200\ \mu m$; recess size, 0.03 μm; recess mesh, 0.01 μm; $c_A^O = 1$ mM.

The position in the matrix of the $\alpha K'\beta c_{B,X}$ terms (corresponding to the $K'c_B c_X$ in (A.1−A.5)) is adjusted in order to maximize the weight of the diagonal of the matrix (a). It has been observed that this disposition allows the convergence of the calculations even for very low values of c_X (for which the formulation b does not reach the convergence criteria).

APPENDIX 2

Short Electrode Validation. The Harriman et al.[39] result for the E reaction study is taken as the reference value, and the analytical approximations of Levich (A.10),[43] Newman (A.11),[40] and Aoki (A.12).[47]

$$I_0 = 0.8075P_S^{1/3} \quad (A.10)$$

$$I_0 = 0.8075P_S^{1/3} + 0.7058P_S^{-1/6} - 0.1094P_S^{-1/3} \quad (A.11)$$

$$I_0 = 0.8075P_S^{1/3} + 0.4558P_S^{-1/6} - 0.1984P_S^{-1/3} \quad (A.12)$$

The current values for the simulated geometry are listed in Table 2. The error compared with the Harriman et al. results is

(47) Aoki, K.; Toduka, K.; Matsuda, H. *J. Electroanal. Chem.* **1987**, *217*, 33−47.

−0.02%. Furthermore, apart from the Levich value, the simulated current I_0 is within 1% error.

The study of the E reaction also allows evaluation of the effect of mesh parameters on the model. First, it is worth noting that the mesh size is refined near the electrode edges (geometric progression on a 1-μm path). The mesh size on the electrode edge is kept equal to the mesh size on the recess. On the center of the electrode (from 1 to 9 μm), the mesh is regular. Referring to Table 3, the size of the recess should not exceed 0.03 μm (0.3% of the electrode length) if an error of less than 1% is required. A mesh of 0.03 μm at the edges of the electrode (and on the recess) is found to be acceptable. Concerning the middle of the electrode (Table 4), there is no need to mesh in a very thin manner (20 subdivisions).

Long Electrode Validation. Due to the large size of the electrode, the effect of the recess size and the recess mesh is considerably diminished, resulting in a total error of −0.3% for a recess and a recess mesh size of 0.1 μm. Furthermore, as the electrode size is increased, the effect of the middle electrode mesh is stronger. Nevertheless, the bigger mesh is chosen (mesh size of 4.9 μm with 0.26% error on the current value I_0). Finally, the mesh at the end of the channel has been also assessed and no particular effect on the precision of the concentration values is highlighted (data not shown).